Oxysulfide photocatalyst for visible-light-driven overall water splitting

Qian Wang[1,9], Mamiko Nakabayashi[2], Takashi Hisatomi[3], Song Sun[4,5], Seiji Akiyama[6,7], Zheng Wang[3], Zhenhua Pan[1], Xiong Xiao[7,8], Tomoaki Watanabe[8], Taro Yamada[1], Naoya Shibata[2], Tsuyoshi Takata[3] and Kazunari Domen[1,3]★

Oxysulfide semiconductors have narrow bandgaps suitable for water splitting under visible-light irradiation, because the electronegative sulfide ions negatively shift the valence band edges of the corresponding oxides[1,2]. However, the instability of sulfide ions during the water oxidation is a critical obstacle to simultaneous evolution of hydrogen and oxygen[3]. Here, we demonstrate the activation and stabilization of $Y_2Ti_2O_5S_2$, with a bandgap of 1.9 eV, as a photocatalyst for overall water splitting. On loading of IrO_2 and Rh/Cr_2O_3 as oxygen and hydrogen evolution co-catalysts, respectively, and fine-tuning of the reaction conditions, simultaneous production of stoichiometric amounts of hydrogen and oxygen was achieved on $Y_2Ti_2O_5S_2$ during a 20 h reaction. The discovery of the overall water splitting capabilities of $Y_2Ti_2O_5S_2$ extends the range of promising materials for solar hydrogen production.

Light-driven water splitting using particulate semiconductor photocatalysts via single photo-excitation is driving down the projected cost of solar hydrogen, potentially to a level that is competitive with fossil-fuel-derived hydrogen because of the simplicity of this system[4,5]. Photocatalytic water-splitting panels retain the intrinsic activity of the photocatalysts and are essentially extensible beyond the scale of square metres[6]. However, to harvest the solar energy efficiently, the development of narrow-bandgap photocatalysts capable of splitting water under visible-light irradiation is critically necessary[7,8]. Metal chalcogenides have shown promise for efficient solar energy harvesting due to their narrow bandgaps[9-11]; however, the water oxidation reaction competes with oxidation of the lattice chalcogen ions[9]. Simultaneous H_2 and O_2 production by CdS nanorods decorated with nanoparticulate reduction and molecular oxidation co-catalysts has been reported[10], but the H_2/O_2 ratio strongly deviated from the stoichiometric value of 2 due to oxidation of the S^{2-} and cysteine ligands by photogenerated holes[10]. Oxysulfides are expected to be more durable against self-oxidation, because the surface S^{2-} ions are stabilized by hybridization of the S-3p and O-2p orbitals[1,2], although the utilization of such oxysulfides for light-driven photocatalytic overall water splitting still remains elusive. Complete suppression of the oxidation of sulfur ions is a challenging task[3] that requires an efficient hole extraction mechanism. Additionally, under neutral conditions, the difference between the oxidation potential of water and the valence band top

for oxysulfides is small[1]. Here, we report promising photocatalytic water-splitting activity for $Y_2Ti_2O_5S_2$, which responds to a large portion of the solar spectrum owing to its narrow bandgap (1.9 eV), and directly decomposes water into hydrogen and oxygen in a stoichiometric ratio.

The $Y_2Ti_2O_5S_2$ unit cell comprises alternating rocksalt slabs $[Y_2S_2]^{2+}$ and ReO_3-type blocks formed from -(TiO$_2$)–(O)–(TiO$_2$)- layers stacked along the c direction (Fig. 1a)[12,13]. The X-ray diffraction (XRD) pattern for the $Y_2Ti_2O_5S_2$ synthesized through a solid-state reaction indicates a single $Y_2Ti_2O_5S_2$ phase with tetragonal symmetry ($I4/mmm$) (Fig. 1b)[12], which agrees with both the simulated and measured patterns reported in the literature[12,14-16]. The scanning electron microscopy (SEM) image in Fig. 2a reveals that the particle size ranges from several micrometres to 10 μm. Particles 1–2 μm in size are single crystals, whereas larger particles (>2 μm) are secondary particles made up of these primary particles (Fig. 2b,c). Elemental analysis using inductively coupled plasma atomic emission spectroscopy (ICP-AES) and also oxygen/nitrogen and carbon/sulfur analyses showed that the powder composition is Y:Ti:S:O = 2.0:2.0:2.2:5.1, which is close to stoichiometry. The valence states of Y, Ti and S species in $Y_2Ti_2O_5S_2$ were determined by X-ray photoelectron spectroscopy (XPS) to be Y^{3+}, Ti^{4+} and S^{2-}, respectively, consistent with the composition (Supplementary Fig. 1). The oxygen species were attributed to oxidic compounds and adsorbed O_2 and/or ambient moisture[17].

$Y_2Ti_2O_5S_2$ absorbs light with wavelength up to 650 nm, as shown by the diffuse reflectance spectrum (DRS) in Fig. 3a. The bandgap is estimated to be 1.9 eV from the onset wavelength in the DRS. Mott–Schottky plots and current–potential profiles for $Y_2Ti_2O_5S_2$ electrodes (Fig. 3b and Supplementary Figs. 2 and 3) exhibit positive slopes and photoanodic current characteristics of n-type semiconductors, respectively, similar to analogous oxysulfides, as exemplified by $Sm_2Ti_2O_5S_2$ (ref. [1]). The flat-band potential of $Y_2Ti_2O_5S_2$ was estimated to be −1.05 V versus the normal hydrogen electrode (NHE) and was almost independent of pH in the range of 5–13, unlike metal oxides[1]. Similar behaviour was observed for $Sm_2Ti_2O_5S_2$ and BiCuOS and is indicative of a small acid dissociation constant for hydroxyl groups on the $Y_2Ti_2O_5S_2$ surface[1,18]. Hence, the conduction band minimum (CBM) for $Y_2Ti_2O_5S_2$ was determined to lie between −1.1 and −1.0 V versus NHE given a potential difference

Fig. 1 | Structure of $Y_2Ti_2O_5S_2$. a, Crystal structure of $Y_2Ti_2O_5S_2$. **b**, XRD pattern for as-prepared $Y_2Ti_2O_5S_2$ (red spectra) and simulated data[14] (black spectra) for comparison.

of $0-0.1$ V between the flat-band potential and the CBM in n-type oxysulfides[1]. From the bandgap energy, the valence band maximum (VBM) was estimated to be $0.8-0.9$ V versus NHE. This is in good agreement with that obtained by photoelectron spectroscopy in air (PESA) (-5.2 eV versus vacuum, Supplementary Fig. 4). According to the proposed band structure (Fig. 3c), in mildly alkaline (for example, pH 9) solutions, the CBM is more negative than the reduction potential of water to produce H_2, while the VBM is more positive than the oxidation potential of water to produce O_2. Thus, $Y_2Ti_2O_5S_2$ meets the thermodynamic requirements for photocatalytic water splitting for pH values around $8-9$. The partial density of states (PDOS) computed using CASTEP is presented in Fig. 3d and Supplementary Fig. 5. The CBM for $Y_2Ti_2O_5S_2$ consists predominately of Ti-3d orbitals, while the VBM is composed of O-2p, S-3p and Y-3d orbitals. The S-3p band strongly overlaps with states due to O-2p orbitals, implying significant hybridization between S and O atoms. In addition, $Y_2Ti_2O_5S_2$ exhibits a more negative VBM than $Sm_2Ti_2O_5S_2$ (2.1 eV)[1,2], suggesting that Y-3d orbitals also contribute to the VBM[2].

The $Y_2Ti_2O_5S_2$ was decorated by adsorption of IrO_2 as an oxygen evolution co-catalyst (OEC). As a hydrogen evolution co-catalyst (HEC) and surface modification for HEC, core/shell Rh/Cr_2O_3 was deposited subsequently by two-step photodeposition using Rh^{3+} and Cr^{6+} species. The functionality of the IrO_2 and Rh species on $Y_2Ti_2O_5S_2$ was evaluated by oxygen evolution reactions in an aqueous $AgNO_3$ solution and hydrogen evolution reactions in an aqueous $Na_2S-Na_2SO_3$ solution, respectively (Supplementary Fig. 6). In strong agreement with absorption onset in the DRS, both H_2 and O_2 generation were observed up to 640 nm (Fig. 4a,b), indicating that the photoreactions proceeded via bandgap transitions. The apparent quantum yield (AQY) at wavelengths of $420-480$ nm was $5.3 \pm 0.3\%$ and $2.3 \pm 0.1\%$ for H_2 and O_2 production, respectively. The photocatalytic water-splitting activity of $Cr_2O_3/Rh/IrO_2$-loaded $Y_2Ti_2O_5S_2$ was independent of the background pressure (Supplementary Fig. 7) because the Cr_2O_3 shell serves as a diffusion barrier to prevent backward reactions on the noble metal surface during the reaction[19].

Stoichiometric evolution of H_2 and O_2 occurred over $Cr_2O_3/Rh/IrO_2$-loaded $Y_2Ti_2O_5S_2$ in distilled water buffered by La_2O_3 (pH 8.5) under visible-light irradiation ($\lambda > 420$ nm) (Fig. 5a). Cr_2O_3/Rh-loaded $Y_2Ti_2O_5S_2$ also produced H_2 and O_2 under the same conditions (Supplementary Fig. 8). However, the H_2/O_2 ratio deviated from the stoichiometric value of 2, probably due to oxidation of

S^{2-} in $Y_2Ti_2O_5S_2$, which competes with the water oxidation reaction, as observed for other metal chalcogenides[9,10]. Loading with the IrO_2 OEC is therefore necessary to stably oxidize water to O_2 (refs. [10,20,21]). In addition, $Y_2Ti_2O_5S_2$ loaded only with IrO_2 exhibited negligible H_2 and O_2 evolution in water buffered with La_2O_3, indicating the need for co-loading with both the HEC and OEC. Isotopic labelling using $H_2^{18}O$ (97 at% ^{18}O) as a reactant confirmed that the ratio of ^{18}O atoms in the O_2 generated over $Cr_2O_3/Rh/IrO_2$-loaded $Y_2Ti_2O_5S_2$ was ~97% after a 3 h reaction (Supplementary Fig. 9). Thus, the O_2 was produced from water.

The Cr_2O_3/Rh co-catalyst nanocomposites were deposited on different regions of the $Y_2Ti_2O_5S_2$ to the IrO_2 nanoparticles (Supplementary Table 1 and Supplementary Figs. 10 and 11). This is because the photodeposition method allows selective deposition of Cr_2O_3/Rh nanoparticles on reduction sites and the IrO_2 nanoparticles function as oxidation sites. XPS analysis (Supplementary Fig. 12) revealed that the Ir, Rh and Cr species on the surface of $Y_2Ti_2O_5S_2$ had valence states attributable to IrO_2, metallic Rh and Cr_2O_3, respectively. This indicates successful deposition of Cr_2O_3/Rh on $Y_2Ti_2O_5S_2$ without blocking the pre-loaded IrO_2 nanoparticles or changing the oxidation state of IrO_2. Notably, $Y_2Ti_2O_5S_2$ powder loaded first with Cr_2O_3/Rh and then with IrO_2 split water 30% less efficiently than that loaded with IrO_2 and then Cr_2O_3/Rh (Supplementary Fig. 13) because the IrO_2 was deposited non-selectively and covered part of the Cr_2O_3/Rh HEC. This result suggests that the HEC and OEC should be co-loaded on one single photocatalyst particle but on different regions to promote the overall water-splitting activity effectively.

The photocatalytic activity of the $Cr_2O_3/Rh/IrO_2$-loaded $Y_2Ti_2O_5S_2$ varied significantly with the pH of the reaction solution (Fig. 5b). Stoichiometric H_2 and O_2 evolution occurred in the pH range of $8-9$, indicating that the rates of the O_2 and H_2 evolution reactions were balanced at this pH. The difference between the water-oxidation potential and the VBM potential of $Y_2Ti_2O_5S_2$ in pure water (pH 6.8) seems to be too small to drive the water oxidation reaction efficiently. This was confirmed by the fact that a negligible amount of oxygen was evolved over IrO_2-loaded $Y_2Ti_2O_5S_2$ in an $AgNO_3$ aqueous solution at neutral pH. On the other hand, the XPS results in Supplementary Fig. 14 show that the Cr_2O_3 shell was partially dissolved at pH 10, resulting in a strong back reaction on the exposed Rh nanoparticles. Therefore, careful tuning of the pH of the reactant is vital for achieving water splitting over
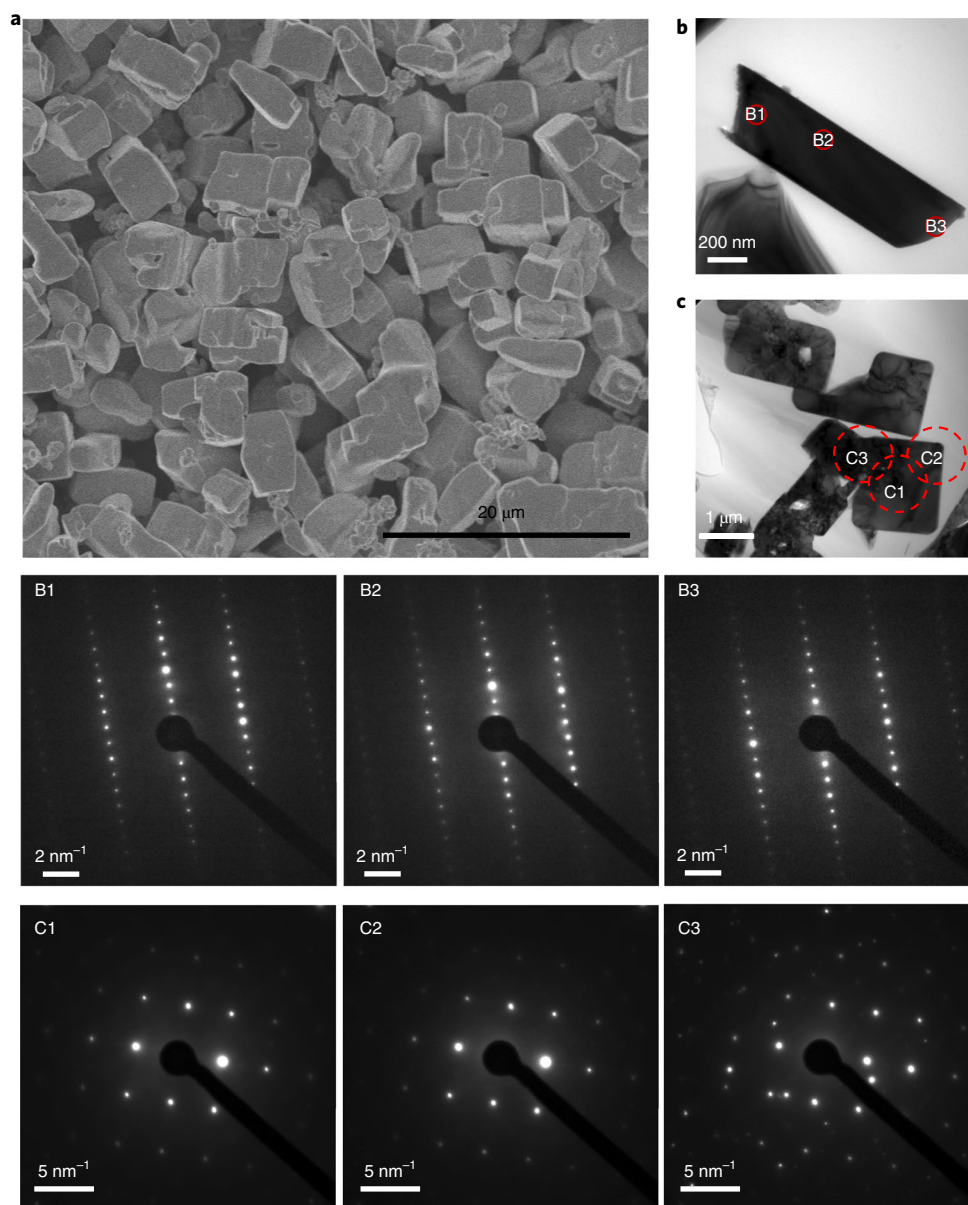
Fig. 2 | Morphology of $Y_2Ti_2O_5S_2$. a, SEM image of as-prepared $Y_2Ti_2O_5S_2$ powder. **b,c**, High-resolution transmission electron microscopy (HRTEM) images and corresponding selected area electron diffraction (SAED) patterns (bottom two rows) for $Y_2Ti_2O_5S_2$ particles with size of ~1 μm and thickness of ~0.4 μm (**b**) and $Y_2Ti_2O_5S_2$ particles larger than 2 μm (**c**).

Cr_2O_3/Rh/IrO_2-loaded $Y_2Ti_2O_5S_2$. The catalysts collected after a 6 h reaction in an aqueous NaOH solution at pH 9 were examined. The XRD patterns reveal that the crystallinity of the $Y_2Ti_2O_5S_2$ was essentially unchanged (Supplementary Fig. 15). Furthermore, the bulk $Y_2Ti_2O_5S_2$ was confirmed to have a stoichiometric elemental ratio of Y:Ti:S:O = 2.0:2.0:2.0:5.1 after the reaction. The binding energies of the Y-3*d*, Ti-2*p*, S-2*p*, S-2*s* and O-1*s* peaks and the proportions of surface Ti, S and O species did not undergo large changes either (Supplementary Fig. 1 and Supplementary Table 2). These results, along with the isotopic labelling experiment and the numbers of outmost sulfide and oxide ions (see Supplementary Information), indicate that hydrogen and oxygen generation over Cr_2O_3/Rh/IrO_2-loaded $Y_2Ti_2O_5S_2$ powder are due not to self-oxidation of S^{2-} species on $Y_2Ti_2O_5S_2$ but to water splitting.

As discussed above, the particle size in the $Y_2Ti_2O_5S_2$ calcined at 1,073 K ranged from several micrometres to 10 μm. Although the particles were well crystallized, excessively large particles are

unfavourable in photocatalytic reactions because photoexcited carriers have to migrate a long distance to reach active sites on the surface[22]. Moreover, the TEM images in Supplementary Fig. 16 reveal grain boundaries in large particles (>2 μm). Such boundaries trap photoexcited carriers and enhance charge recombination, which lowers the quantum efficiency[23]. Therefore, methods for reducing the $Y_2Ti_2O_5S_2$ particle size were investigated. It was found that smaller particles (<5 μm) of single-phase $Y_2Ti_2O_5S_2$ could be obtained by decreasing the calcination temperature to 973 K (Supplementary Fig. 17). As shown in Fig. 5a, the Cr_2O_3/Rh/IrO_2-loaded $Y_2Ti_2O_5S_2$ synthesized at 973 K generated almost three times as much H_2 and O_2 as the catalyst produced at 1,073 K. The AQYs at 420, 500 and 600 nm were 0.36%, 0.23% and 0.05%, respectively and the solar-to-hydrogen conversion efficiency (STH) was 0.007% (Figs. 4c and 5c).

Stoichiometric evolution of hydrogen and oxygen was confirmed for Cr_2O_3/Rh/IrO_2-loaded $Y_2Ti_2O_5S_2$ powders during the 20 h
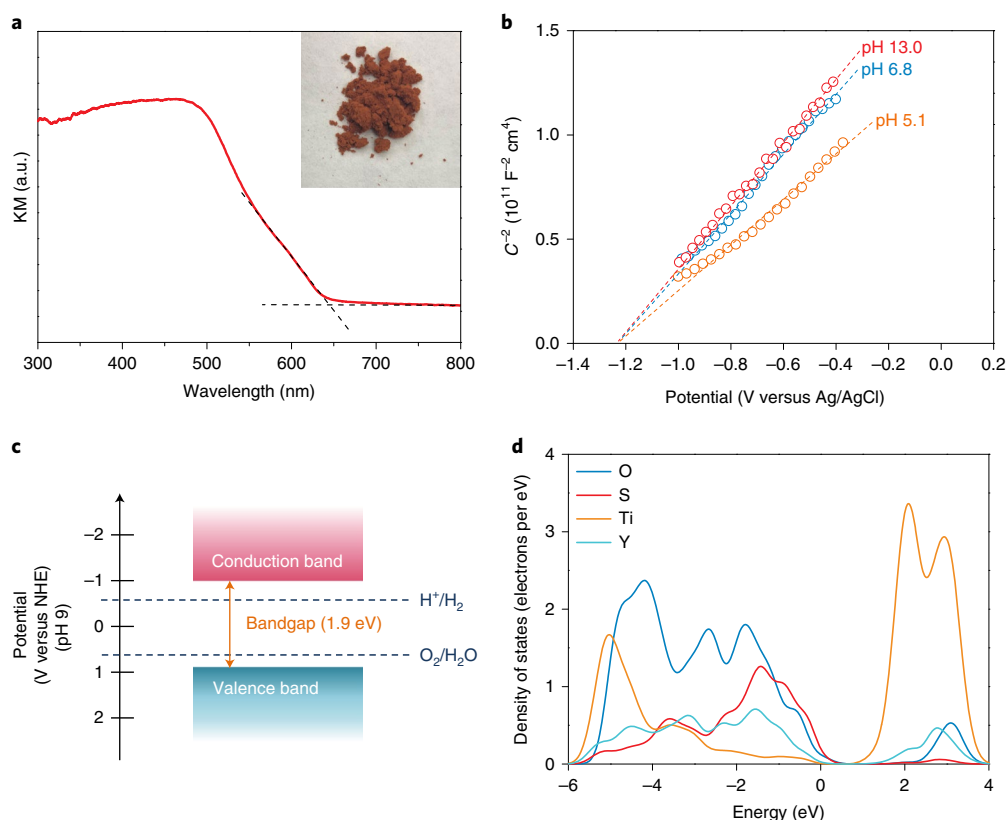
Fig. 3 | Band structure of $Y_2Ti_2O_5S_2$. a, DRS for $Y_2Ti_2O_5S_2$. KM, Kubelka–Munk model (see Methods). Inset, photograph of the $Y_2Ti_2O_5S_2$ powder. **b**, Mott–Schottky plots for an $Y_2Ti_2O_5S_2$ electrode in 0.1 M Na_2SO_4 at pH 5.1 (orange symbols), pH 6.8 (blue symbols) and pH 13.0 (red symbols). **c**, Schematic band structure diagram for $Y_2Ti_2O_5S_2$. **d**, DOS for O (blue line), S (red line), Ti (orange line) and Y (light blue line).
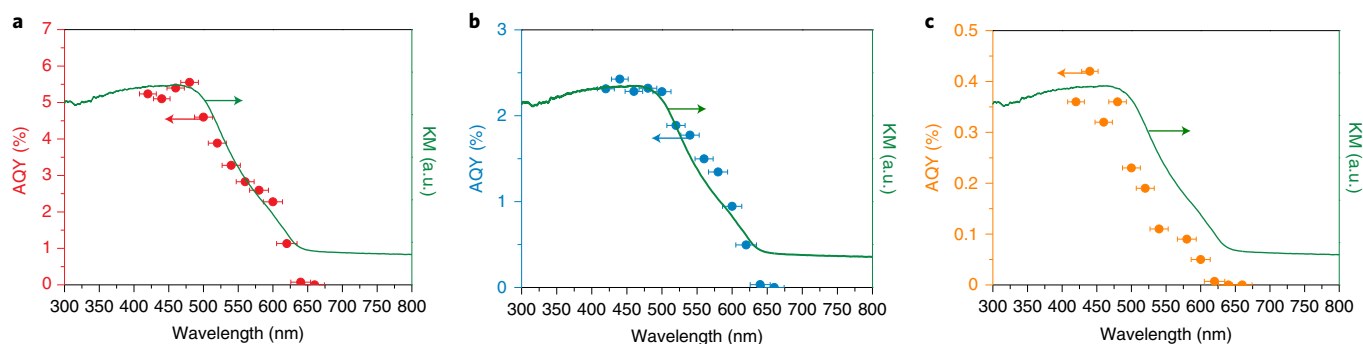

Fig. 4 | Wavelength dependence of photocatalytic activity of $Y_2Ti_2O_5S_2$. a–c, Dependence of AQY for hydrogen production using $Y_2Ti_2O_5S_2$ loaded with 3 wt% Rh (**a**), oxygen production using $Y_2Ti_2O_5S_2$ loaded with 1 wt% IrO_2 (**b**) and overall water splitting using Cr_2O_3/Rh/IrO_2-modified $Y_2Ti_2O_5S_2$ (**c**) on incident light wavelength, along with DRS of $Y_2Ti_2O_5S_2$ for comparison (green line). The hydrogen evolution reactions were carried out in aqueous solutions of Na_2S–Na_2SO_3 (20 mM each). The oxygen evolution reactions were carried out in aqueous solutions of $AgNO_3$ (20 mM) buffered by La_2O_3 (pH 8.5). The $Y_2Ti_2O_5S_2$ for the hydrogen and oxygen evolution reactions was synthesized at 1,073 K. The overall water-splitting reactions were carried out in distilled water buffered by La_2O_3 (pH 8.5). The amounts of IrO_2, Rh and Cr were 0.3, 2 and 1.5 wt%, respectively, for the overall water-splitting reaction. The $Y_2Ti_2O_5S_2$ for the overall water-splitting reactions was synthesized at 973 K. The reactions were performed under illumination from a xenon lamp (300 W) and various bandpass filters.

reaction (Fig. 5d). The photocatalyst retained 81% of the initial water splitting activity in the second run. The thermogravimetric (TG) analysis results in Supplementary Fig. 18 indicate that the $Y_2Ti_2O_5S_2$ remains stable up to 700 °C in both air and N_2. The considerable mass loss at ~600 °C that is typical of oxysulfides due to evaporation of sulfur is not observed for $Y_2Ti_2O_5S_2$ (ref. [18]). This implies that the S atoms in $Y_2Ti_2O_5S_2$ are relatively stable, and holes near the VBM can be employed for water oxidation with the assistance

of the OEC, rather than self-oxidation of S^{2-}. However, as shown in Supplementary Fig. 19, defects such as dislocations still exist in the bulk $Y_2Ti_2O_5S_2$, working as recombination centres of photo-excited charges[24,25]. There is therefore much room for improvement of the efficiency by controlling the particle size and morphology, reducing the defect density through refinement of the material preparation method, managing the selective deposition of the dual co-catalysts, and valence band engineering via doping and forming solid solution.
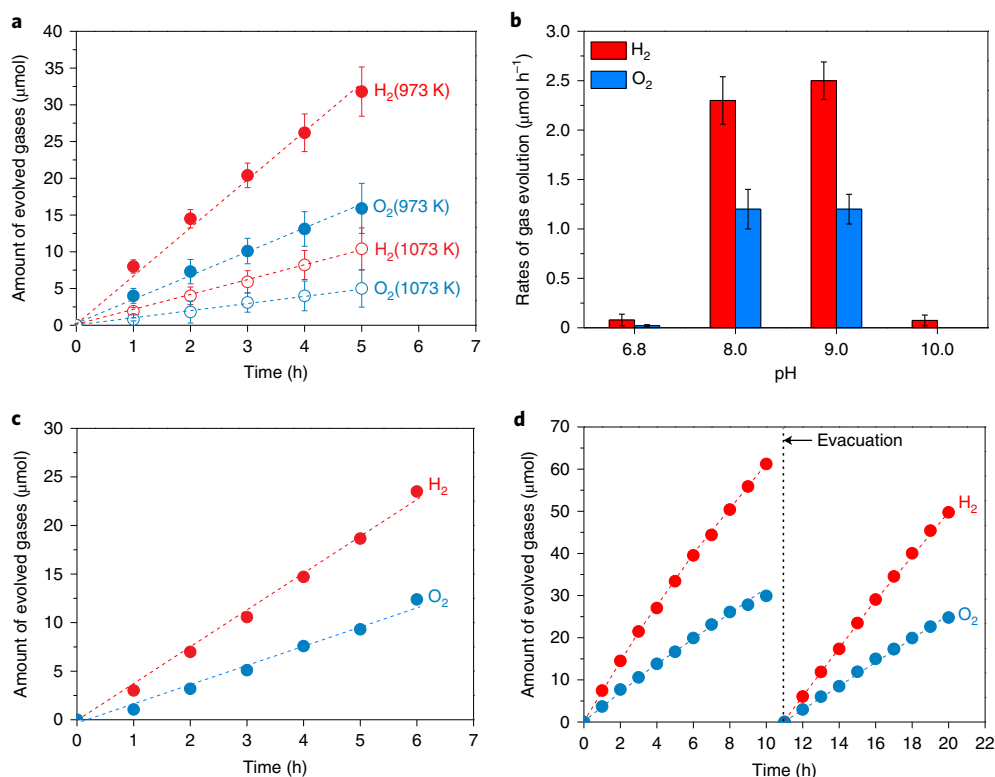
Fig. 5 | Photocatalytic performance of $Y_2Ti_2O_5S_2$ for overall water splitting. a, Time courses of water-splitting reaction on Cr_2O_3/Rh/IrO_2-modified $Y_2Ti_2O_5S_2$ in distilled water buffered by La_2O_3 (pH 8.5). The $Y_2Ti_2O_5S_2$ was synthesized at 1,073 K (open symbols) and 973 K (filled symbols). **b**, Dependence of gas evolution rates on Cr_2O_3/Rh/IrO_2-loaded $Y_2Ti_2O_5S_2$ on the pH of the reaction solution. The $Y_2Ti_2O_5S_2$ was synthesized at 1,073 K. The above reactions were carried out under illumination from a xenon lamp (300 W, $\lambda > 420\,nm$). Error bars in **a** and **b** indicate standard deviation. **c**, Time course of overall water splitting on Cr_2O_3/Rh/IrO_2-modified $Y_2Ti_2O_5S_2$ in distilled water buffered by La_2O_3 (pH 8.5) under simulated sunlight (AM 1.5G). The $Y_2Ti_2O_5S_2$ was synthesized at 973 K. **d**, Time course of overall water splitting on Cr_2O_3/Rh/IrO_2-modified $Y_2Ti_2O_5S_2$ in distilled water buffered by La_2O_3 (pH 8.5) under illumination from a xenon lamp (300 W, $\lambda > 420\,nm$) for 20 h, with evacuation every 10 h (dashed line). The $Y_2Ti_2O_5S_2$ was synthesized at 973 K.

The stability could be improved by replacing IrO_2 with other more effective OECs to inhibit the oxidation of Cr^{3+} in Cr_2O_3 and S^{2-} on the $Y_2Ti_2O_5S_2$ surface[26].

We demonstrated that an oxysulfide semiconductor photocatalyst, $Y_2Ti_2O_5S_2$, evolved H_2 and O_2 via a water-splitting reaction under visible-light irradiation. Following spatially separated loading of IrO_2 and Cr_2O_3/Rh as the OEC and HEC, respectively, and fine-tuning the pH of the reactant, photocatalytic water splitting into H_2 and O_2 in a stoichiometric ratio was achieved. The discovery of an oxysulfide photocatalyst with a narrow bandgap that is applicable in both one-step and Z-scheme water-splitting systems opens new opportunities for research into solar energy conversion.

Online content

Any methods, additional references, Nature Research reporting summaries, source data, statements of code and data availability and associated accession codes are available at https://doi.org/10.1038/s41563-019-0399-z.

References

1. Ishikawa, A. et al. Oxysulfide $Sm_2Ti_2S_2O_5$ as a stable photocatalyst for water oxidation and reduction under visible light irradiation ($\lambda \leq 650\,nm$). *J. Am. Chem. Soc.* **124**, 13547–13553 (2002).
2. Ishikawa, A. et al. Oxysulfides $Ln_2Ti_2S_2O_5$ as stable photocatalysts for water oxidation and reduction under visible-light irradiation. *J. Phys. Chem. B* **108**, 2637–2642 (2004).
3. Fujito, H. et al. Layered perovskite oxychloride Bi_4NbO_8Cl: a stable visible light responsive photocatalyst for water splitting. *J. Am. Chem. Soc.* **138**, 2082–2085 (2016).
4. Shaner, M. R., Atwater, H. A., Lewis, N. S. & McFarland, E. W. A comparative technoeconomic analysis of renewable hydrogen production using solar energy. *Energy Environ. Sci.* **9**, 2354–2371 (2016).
5. Bala, C. R., Breen, S., Shao, Y., Ardo, S. & Weber, A. Z. Evaluating particle-suspension reactor designs for Z-scheme solar water splitting via transport and kinetic modeling. *Energy Environ. Sci.* **11**, 115–135 (2018).
6. Goto, Y. et al. A particulate photocatalyst water-splitting panel for large-scale solar hydrogen generation. *Joule* **2**, 509–520 (2018).
7. Sivula, K. & van de Krol, R. Semiconducting materials for photoelectrochemical energy conversion. *Nat. Rev. Mater.* **1**, 15010 (2016).
8. Tachibana, Y., Vayssieres, L. & Durrant, J. R. Artificial photosynthesis for solar water-splitting. *Nat. Photon.* **6**, 511–518 (2012).
9. Ellis, A. B., Kaiser, S. W., Bolts, J. M. & Wrighton, M. S. Study of n-type semiconducting cadmium chalcogenide-based photoelectrochemical cells employing polychalcogenide electrolytes. *J. Am. Chem. Soc.* **99**, 2839–2848 (1977).
10. Wolff, C. M. et al. All-in-one visible-light-driven water splitting by combining nanoparticulate and molecular co-catalyst on CdS nanorods. *Nat. Energy* **3**, 862–869 (2018).
11. Ran, J., Zhang, J., Yu, J., Jaroniec, M. & Qiao, S. Earth-abundant cocatalysts for semiconductor-based photocatalytic water splitting. *Chem. Soc. Rev.* **43**, 7787–7812 (2014).
12. Denis, S. G. & Clarke, S. J. Two alternative products from the intercalation of alkali metals into cation-defective Ruddlesden–Popper oxysulfides. *Chem. Commun.* **22**, 2356–2357 (2001).
13. Hyett, G. et al. Electronically driven structural distortions in lithium intercalates of the $n = 2$ Ruddlesden–Popper-type host $Y_2Ti_2O_5S_2$: synthesis, structure and properties of $Li_xY_2Ti_2O_5S_2$ ($0 < x < 2$). *J. Am. Chem. Soc.* **126**, 1980–1991 (2004).
14. Kristin, P. *Materials Data on $Y_2Ti_2S_2O_5$ (SG:139) by Materials Project* (Lawrence Berkeley National Lab, 2016); https://doi.org/10.17188/1200585

15. Oki, H. & Takagi, H. $Y_2Ti_2O_5S_2$ as a high performance anode material for Li ion batteries. *Solid State Ion.* **276**, 80–83 (2015).
16. Rutt, O. J., Hill, T. L., Gál, Z. A., Hayward, M. A. & Clarke, S. J. The cation-deficient Ruddlesden-Popper oxysulfide $Y_2Ti_2O_5S_2$ as a layered sulfide: topotactic potassium intercalation to form $KY_2Ti_2O_5S_2$. *Inorg. Chem.* **42**, 7906–7911 (2003).
17. Ingo, G., Paparazzo, E., Bagnarelli, O. & Zacchetti, N. XPS studies on cerium, zirconium and yttrium valence states in plasma-sprayed coatings. *Surf. Interface Anal.* **16**, 515–519 (1990).
18. BaQais, A. et al. Bismuth silver oxysulfide for photoconversion applications: structural and optoelectronic properties. *Chem. Mater.* **29**, 8679–8689 (2017).
19. Maeda, K. et al. Noble-metal/Cr_2O_3 core/shell nanoparticles as a cocatalyst for photocatalytic overall water splitting. *Angew. Chem. Int. Ed.* **118**, 7970–7973 (2006).
20. Gu., J. et al. Water reduction by a p-$GaInP_2$ photoelectrode stabilized by an amorphous TiO_2 coating and a molecular cobalt catalyst. *Nat. Mater.* **15**, 456–460 (2016).
21. Vequizo, J. J. M., Hojamberdiev, M., Teshima, K. & Yamakata, A. Role of CoO_x cocatalyst on Ta_3N_5 photocatalysts studied by transient visible to mid-infrared absorption spectroscopy. *J. Photochem. Photobiol. C* **358**, 315–319 (2018).
22. Kato, H., Asakura, K. & Kudo, A. Highly efficient water splitting into H_2 and O_2 over lanthanum-doped $NaTaO_3$ photocatalysts with high crystallinity and surface nanostructure. *J. Am. Chem. Soc.* **125**, 3082–3089 (2013).
23. Sherkar, T. S. et al. Recombination in perovskite solar cells: significance of grain boundaries, interface traps and defections. *ACS Energy Lett.* **2**, 1214–1222 (2017).
24. Inoue, Y. Photocatalytic water splitting by RuO_2-loaded metal oxides and nitrides with d^0- and d^{10}-related electronic configurations. *Energy Environ. Sci.* **2**, 364–386 (2009).
25. Kibria, M. G. et al. Visible light-driven efficient overall water splitting using p-type metal-nitride nanowire arrays. *Nat. Commun.* **6**, 6797 (2015).
26. Lyu, H. et al. An Al-doped $SrTiO_3$ photocatalyst maintaining sunlight-driven overall water splitting activity for over 1,000 h of constant illumination. *Chem. Sci.* **10**, 3196–3201 (2019).

Acknowledgements

Author contributions

Q.W. and K.D. designed the research. Q.W. prepared $Y_2Ti_2O_5S_2$ powder and conducted XRD, DRS, XPS, PESA and SEM characterizations, and the water-splitting reactions. Q.W. and T.Y. carried out the isotopic labelling experiment. M.N. and N.S. conducted cross-sectional cutting of particles along with the STEM, STEM-EDS, TEM-EDS, HRTEM and SAED analyses. S.S. performed the theoretical calculations. S.A. carried out the TG analysis. Q.W. and Z.P. fabricated the electrodes by the particle transfer method and conducted the Mott–Schottky measurements. X.X. and T.W. prepared the electrodes using the roll press method. Z.P. and X.X. carried out the photoelectrochemical measurements. T.Y. supervised the elemental analysis. K.D. and T.H. supervised the experimental work. Q.W., T.H., Z.W., T.Y., T.T. and K.D. discussed the results. Q.W., T.H. and K.D. wrote the manuscript with contributions from the other authors.

Competing interests

The authors declare no competing interests.

Additional information

Supplementary information is available for this paper at https://doi.org/10.1038/s41563-019-0399-z.

Reprints and permissions information is available at www.nature.com/reprints.

Correspondence and requests for materials should be addressed to K.D.

Publisher's note: Springer Nature remains neutral with regard to jurisdictional claims in published maps and institutional affiliations.

Methods

Synthesis of $Y_2Ti_2O_5S_2$. The $Y_2Ti_2O_5S_2$ powder was prepared by a solid-state reaction. Y_2O_3 (Wako Pure Chemical Industries, 99.99%), Y_2S_3 (High Purity Chemicals, 99.9%) and TiO_2 (Rare Metallic, 99.99%) were mixed at a ratio of 1:2:6 in an argon-filled recirculating glovebox with an O_2 concentration of less than 3 ppm. The dew point was lower than 193 K. To obtain a sulfur-rich environment during the reaction, sulfur powder (High Purity Chemicals, 99.99%, 5 wt% with respect to the total of the other starting materials) was added to the precursor. The resulting mixture was sealed in an evacuated quartz tube and calcined in a muffle furnace. The calcination temperature was increased from room temperature to 773 K at a rate of 5 K min^{-1}, elevated to 873–1,073 K at 1 K min^{-1}, and maintained at the target value for 96 h before natural cooling. To remove the sulfur species adsorbed on the surface, the $Y_2Ti_2O_5S_2$ powder was annealed in air at 473 K for 1 h, thoroughly rinsed with distilled water and dried in vacuum at 313 K.

Characterization. The XRD patterns for the samples were recorded with a Rigaku SmartLab diffractometer using a Cu Kα source operated at 40 kV and 30 mA. DRS measurements were made using an ultraviolet–visible–near–infrared spectrometer (V-670, JASCO) and were converted from reflectance into the Kubelka–Munk (KM) function. PESA was carried out using a surface analyser (Riken-Keiki, AC-3). XPS measurements were performed using a monochromatic Mg Kα source ($h\nu = 1,253.6$ eV) excited at 8 kV and 10 mA. The analysis chamber pressure was on the order of 1×10^{-6} Pa. The binding energies were corrected using the C 1s peak (285.0 eV) as a reference. The SEM images were obtained using a Hitachi SU8020 system operated at an acceleration voltage of 5 kV. Scanning transmission electron microscope (STEM), scanning transmission electron microscope and energy-dispersive X-ray spectroscopy (STEM-EDS) mapping, HRTEM images and SAED patterns were recorded using a JEM-2800 system (JEOL). Cross-sectional cuts of the particles were prepared using an ion slicer (EM-09100IS, JEOL). Subsequently, a NanoMill Model 1040 (Fichione Instruments) was applied to remove the amorphous damage layer on TEM specimens prepared by the ion beam. TEM-EDS was performed using an X-MAX 100TLE SDD detector (Oxford Instruments). Elemental analysis of the $Y_2Ti_2O_5S_2$ powder was conducted using ICP-AES (ICPS-8100, Shimazu), an EMGA 620 W oxygen/nitrogen analyser (HORIBA) and an EMIA 220 V carbon/sulfur analyser (HORIBA). TG analysis (Thermo plus EVO2, Rigaku Corporation) was conducted to examine the thermal stability of $Y_2Ti_2O_5S_2$, monitoring the total mass loss from ambient temperature to 700 °C in static air and N_2 at a heating rate of 10 °C min^{-1}.

Theoretical calculations. The DOS and related calculations for $Y_2Ti_2O_5S_2$ were performed using the Cambridge Serial Total Energy Package (CASTEP) code based on density functional theory[27,28]. The generalized gradient approximation of Perdew–Burke–Ernzerhof as implemented in the CASTEP code was adopted for the exchange-correlation functional. The calculations were carried out on the following basis: (1) an ultra-soft pseudopotential description of electron–ion interactions represented in reciprocal space, (2) a finite plane-wave basis set with corrections for the description of the wavefunction, truncated at a cutoff energy of 340 eV, (3) an iterative scheme for self-consistent electronic minimization, using a convergence tolerance of 1.0×10^{-6} eV atom^{-1}. During the calculations, the DOS incorporated a $7 \times 7 \times 1$ Monkhorst–Pack k-vector grid for the irreducible part of the first Brillouin zone with a 25 k-vector set. For geometry optimization of the crystal structure, the Broyden–Fletcher–Goldfarb–Shanno algorithm was applied with the following convergent tolerances: the changes in energy ΔE, the maximum force, the maximum stress and the maximum displacement were 1×10^{-5} eV atom^{-1}, 0.03 eV Å^{-1}, 0.05 GPa and 0.001 Å, respectively.

Mott–Schottky measurements. Electrodes of $Y_2Ti_2O_5S_2$ were fabricated by a particle transfer method[29]. $Y_2Ti_2O_5S_2$ powder (60 mg) was suspended in isopropanol (99.9%, 0.5 ml) and dropcast onto a glass substrate (~3×3 cm). After drying at room temperature, a thin titanium layer was deposited by sputtering (MPS-254, ULVAC KIKO) to a thickness of 3 μm to ensure continuity and conductivity. Electrochemical impedance spectroscopy was performed using a three-electrode configuration with an Ag/AgCl reference electrode (in a saturated KCl aqueous solution) and a Pt wire counter-electrode. An aqueous solution of 0.1 M Na_2SO_4 was used as the electrolyte, and was stirred and purged with Ar gas. The pH of the electrolyte solution was adjusted by adding H_2SO_4 (aq.) or NaOH (aq.) when necessary. Before the impedance spectroscopy test, cyclic voltammetry was carried out at a scan rate of 10 mV s^{-1}. The impedance spectra were recorded at a frequency of 1 kHz unless otherwise noted, with an a.c. amplitude of 10 mV under darkness.

Photoelectrochemical measurements. The $Y_2Ti_2O_5S_2$ electrodes were fabricated by the particle transfer method presented above and a roll press method. In the particle transfer method, the Ti and Au layers, 1 and 3 μm thickness, respectively, were deposited by vacuum evaporation in sequence. In the roll press method, $Y_2Ti_2O_5S_2$ powder (6 mg) was dispersed in 0.5 ml of isopropanol. The powder ink was then dropcast on a 1×2 cm Ti substrate (Nilaco). The electrode was fabricated using a roll-to-roll machine (Yoshida Kinen, 25/100-2H) with a force of 9 kN. The IrO_2 co-catalyst was coated on the $Y_2Ti_2O_5S_2$/Ti electrode by dropping 150 μl

IrO_2 colloid (0.05 mg ml^{-1}) onto the surface. Electrical contact was established by embedding a copper wire in indium (Nilaco) at the bottom or back of the sample. The copper wire and indium were coated with epoxy (Araldite).

Photoelectrochemical water splitting properties were investigated in the three-electrode configuration using a Ag/AgCl reference electrode (in saturated KCl aqueous solution) and a Pt wire counter-electrode. The potential of the working electrode was controlled by a potentiostat (Hokuto Denko, HSV-100). Potassium phosphate solution (pH 9 and 13) was used as the electrolyte solution under stirring and purging with Ar gas. The photoelectrode was irradiated with a solar simulator (AM 1.5G; Sanei Electric, XES-40S2-CE). Current–potential curves were measured at a scan rate of 10 mV s^{-1} from positive to negative potential. Note that the photoelectrochemical performance has not yet been optimized.

Photocatalytic reactions for hydrogen evolution. In the reactions for producing hydrogen, Na_2S and Na_2SO_3 (20 mM each) were used as sacrificial reagents and were dissolved in 150 ml of distilled water containing a photocatalyst sample (0.3 g). Rh nanoparticles (3 wt%) as HECs were loaded on the $Y_2Ti_2O_5S_2$ powder by photodeposition. A calculated amount of $RhCl_3 \cdot 3H_2O$ (Wako Pure Chemical Industries, 99.9%) was added to the solution and reduced to metallic Rh by photoexcited electrons from the photocatalyst in the initial stage of the reaction (Supplementary Fig. 12). The reactions were conducted in a Pyrex top-irradiation reaction vessel connected to a glass-closed gas circulation system. Argon gas was introduced into the circulation system as a carrier gas after removing the air. The total background pressure of argon and water vapour was ~7 kPa. The temperature of the reactant solution was maintained at 288 K using cooling water. The reactions were performed under irradiation from a 300 W xenon lamp (Lamp House, R300-3J) equipped with a cutoff filter ($\lambda > 420$ nm). The amounts of gas produced were measured by gas chromatography (Shimadzu GC-8A with a thermal conductivity detector, MS-5A columns and argon carrier gas). The reaction rates were determined from a linear regression fit once hydrogen evolution became mostly stable.

Photocatalytic reactions for oxygen evolution. As a co-catalyst for oxygen evolution, IrO_2 nanoparticles (1 wt%) were loaded on the $Y_2Ti_2O_5S_2$ powder through an adsorption process in a colloidal IrO_2 solution. The preparation details for the IrO_2 colloid have been described previously[30]. The as-prepared $Y_2Ti_2O_5S_2$ powder was suspended in an aqueous solution containing the desired amount of IrO_2 colloid and stirred for 40 min. The procedure allowed IrO_2 nanoparticles to be adsorbed onto the $Y_2Ti_2O_5S_2$ surface. The IrO_2-loaded $Y_2Ti_2O_5S_2$ powder was collected by filtration and dried at 313 K under vacuum. For the oxygen evolution reaction, IrO_2-loaded $Y_2Ti_2O_5S_2$ powder (0.3 g) was dispersed in 150 ml of an $AgNO_3$ (20 mM) aqueous solution, where Ag$^+$ cations acted as sacrificial electron acceptors. The reaction trials were performed in the same top-irradiation system at the same temperature and background pressure as the hydrogen evolution reactions. The reaction rate was determined from the amount of oxygen evolved in the first hour.

Photocatalytic reactions for overall water splitting. The $Y_2Ti_2O_5S_2$ powder was added to an aqueous solution containing a calculated amount of the IrO_2 colloid and stirred for 40 min, followed by rinsing with distilled water, filtration and drying at 313 K in vacuum. Subsequently, the IrO_2-loaded $Y_2Ti_2O_5S_2$ powder was dispersed in a Na_2S–Na_2SO_3 (20 mM each) aqueous solution containing the desired amount of $RhCl_3 \cdot 3H_2O$. Photodeposition of the Rh co-catalyst was performed under visible-light illumination ($\lambda > 420$ nm) until steady gas evolution rates were obtained (typically for 2–3 h). After rinsing, filtrating and drying at 313 K in vacuum, the Rh/IrO_2-loaded powder was dispersed in an aqueous methanol solution (10 vol%) containing the desired amount of K_2CrO_4. The resultant suspension was illuminated with visible light ($\lambda > 420$ nm) for 12 h to reduce K_2CrO_4 to Cr_2O_3 (Supplementary Fig. 12). The nominal loading amounts of IrO_2, Rh and Cr were 0.3, 2 and 1.5 wt%, respectively, unless otherwise noted (Supplementary Fig. 20). The final product was washed thoroughly with distilled water, filtrated and then allowed to dry at 313 K in vacuum.

Unless otherwise noted, photocatalytic reactions for overall water splitting were carried out in the same closed gas circulation system with top illumination from a 300 W xenon lamp equipped with a cutoff filter ($\lambda > 420$ nm) that was used for the hydrogen/oxygen evolution measurements. The Cr_2O_3/Rh/IrO_2-loaded $Y_2Ti_2O_5S_2$ (0.2 g) powder was dispersed in 150 ml of distilled water. The pH of the reactant was adjusted by adding La_2O_3 (0.1 g) as a buffer (pH 8.5) or H_2SO_4 (aq.) or NaOH (aq.) when necessary. No gas production was detected in the system containing only La_2O_3 with or without light illumination. Besides, the gas evolution rates did not show large differences from the systems using an aqueous NaOH for pH adjustment and those using La_2O_3 as a buffer (Fig. 5b). Therefore, it can be concluded that the La_2O_3 served only as a buffer for pH adjusting. The reaction vessel was evacuated several times before the reaction to ensure that no air remained. The reaction temperature was kept at 288 K. The background pressure was 7 kPa unless otherwise noted.

Quantum yield measurements. The AQY of the photocatalytic reactions was calculated using

$$\text{AQY}(\%) = (AR/I) \times 100\%$$

where R and I denote the gas evolution rate and the photon flux of monochromatic light, respectively, and A is the number of electrons needed to generate one molecule of H_2 or O_2, that is, 2 or 4 for hydrogen or oxygen evolution, respectively. The water-splitting reaction was carried out using the same experimental set-up described above, except for the use of bandpass filters with central wavelengths of 420.3, 441.3, 460.0, 478.7, 499.7, 518.8, 541.5, 559.5, 582.3, 599.8, 619.8, 639.6 and 658.7 nm and a full-width at half-maximum of 13 ± 1 nm. The number of incident photons illuminating the reaction cell was measured using a grating spectroradiometer.

STH measurement. The water-splitting reaction was conducted under simulated sunlight illumination. The STH is given as

$$STH(\%) = (R(H_2) \times \Delta G_r)/(P \times S) \times 100$$

where $R(H_2)$, ΔG_r, P and S indicate the rate of hydrogen evolution during the water-splitting reaction, the reaction Gibbs energy of the water-splitting reaction, the energy intensity of the AM 1.5G solar irradiation ($100\,mW\,cm^{-2}$) and the irradiated sample area ($38\,cm^2$), respectively.

Isotopic labelling. The water-splitting reaction using ^{18}O-labelled water (water-^{18}O, Aldrich, 97 at% ^{18}O) over $Cr_2O_3/Rh/IrO_2$-loaded $Y_2Ti_2O_5S_2$ under

visible-light irradiation ($\lambda > 420$ nm) was carried out in a small Pyrex cell. The reaction was performed in 5 ml of $H_2{}^{18}O$ containing 0.1 g of $Cr_2O_3/Rh/IrO_2$-loaded $Y_2Ti_2O_5S_2$ and 0.1 g of La_2O_3 (pH 8.5). The amount of gas produced in 3 h was analysed by both gas chromatography and mass spectrometry (Hiden Analytical).

Data availability

The data that support the findings of this study are available from the corresponding author upon reasonable request.

References

27. Milman, V. et al. Electronic structure, properties and phase stability of inorganic crystals: a pseudopotential plane-wave study. *Int. J. Quantum Chem.* **77**, 895–910 (2000).
28. Materials Studio CASTEP (Accelrys, 2001).
29. Minegishi, T., Nishimura, N., Kubota, J. & Domen, K. Photoelectrochemical properties of $LaTiO_2N$ electrodes prepared by particle transfer for sunlight-driven water splitting. *Chem. Sci.* **4**, 1120–1124 (2013).
30. Le, P.-T. C. et al. Photoelectrochemical properties of crystalline perovskite lanthanum titanium oxynitride films under visible light. *J. Phys. Chem. C* **113**, 6156–6162 (2009).